Book of Tutorials and Abstracts

European Microbeam Analysis Society

EMAS 2024

14th

REGIONAL WORKSHOP

on

THE EDGE OF NEW EM AND MICROANALYSIS TECHNOLOGY

12 to 15 May 2024
at the
Brno University of Technology, Brno, Czech Republic

Organised in collaboration with:
Brno University of Technology (VUT)
Central European Institute of Technology (CEITEC)

EMAS
European Microbeam Analysis Society eV
www.microbeamanalysis.eu/

This volume is published by:
European Microbeam Analysis Society eV (EMAS)
EMAS Secretariat
c/o Eidgenössische Technische Hochschule, Institut für Geochemie und Petrologie
Clausiusstrasse 25
8092 Zürich
Switzerland

ISBN 978 90 8227 6978
NUR code: 971 – Materials Science

ACCELERATING MICROANALYSIS IN SEM USING THE BACKSCATTERED ELECTRON AND X RAY (BEX) TECHNIQUE

Philippe T. Pinard and H. Mansour

Oxford Instruments NanoAnalysis
Halifax Road, High Wycombe HP12 3SE, Great Britain
e-mail: philippe.pinard@oxinst.com

Dr Philippe Pinard graduated with a PhD in Engineering from the RWTH Aachen in Germany. He then joined Oxford Instruments NanoAnalysis in 2016 where he is currently the Director of Research and Technology. His research focusses on EDS, WDS and EBSD, in particular the development and improvement of these analytical techniques. He is author or co-author of 72 papers in international journals.

1. INTRODUCTION

A modern scanning electron microscope (SEM) will always be equipped with at least three detectors: secondary electron (SE), backscatter electron (BSE), and energy-dispersive X-ray spectrometry (EDS) detectors. The SE and BSE signals are typically used to navigate around the sample and find areas of interest. BSE signal is often critical in this process as it quickly provides compositional information about the sample. For more detailed compositional information, the EDS detector is then used to detect the element present and measure their composition and spatial distribution.

BSE detectors occupy a prime location in the microscope chamber, being positioned below the pole piece and directly above the sample. This arrangement provides a large solid angle to detect the emitted BSEs from the sample and symmetry with respect to the electron beam to produce images with either compositional or topographical contrast. The BSE signal has a good contrast when the difference in atomic number is high. To detect small changes in atomic number, the gain and offset needs to be adjusted accordingly and the dwell time needs to be increased to reduce noise. In such conditions, the dynamic range will be reduced, and the BSE will not be able to detect high variations in atomic number in addition to the low variations.

A solution to obtain compositional information about the sample is to collect EDS data, which can provide unambiguous chemical element content. Historically, there has been a big difference in the speed of acquisition between BSE and EDS, on one hand BSE imaging typically takes seconds or less, on the other hand EDS collection of a map could take minutes or hours. Since the introduction of silicon drift detectors, the throughput capability of EDS has increased with the advance of large area sensors [1, 2] and faster, low-noise electronics [3, 4]. There is, however, a physical limitation from the ionisation cross-sections that not all electrons entering a sample will generate an X-ray. There is, therefore, more BSEs emitted from a sample than X-rays. Figure 1 shows the ratio between emitted BSEs versus X-rays based on theoretical calculations for pure samples at an accelerating voltage of 20 kV. The ratio is for perfect detectors that would cover the entire hemisphere above the sample. Even with the largest EDS detector, the number of detected X-rays will always be significantly smaller than the number of electrons detected by the BSE detector.

It nevertheless highlights the importance of maximising the solid angle of the EDS detector to detect as many X-rays as possible by using large sensors [1, 2] or positioning the EDS detector as close as possible to the sample [7, 8]. One geometry is to utilise the location of the BSE detector under the pole piece using an annular EDS detector [9], which can lead to 5 - 100x increase in the solid angle [10] with respect to conventional EDS detectors. One drawback is the need of an electron filter to block the SEs and BSEs from entering the EDS sensors [11]. In conventional X-ray detectors, an electron trap is fitted in front of the sensor to deflect the electrons emitted in the direction of the sensor, otherwise electrons would overload the pulse processor, cause background artefacts, and damage the front contact after prolonged exposure.

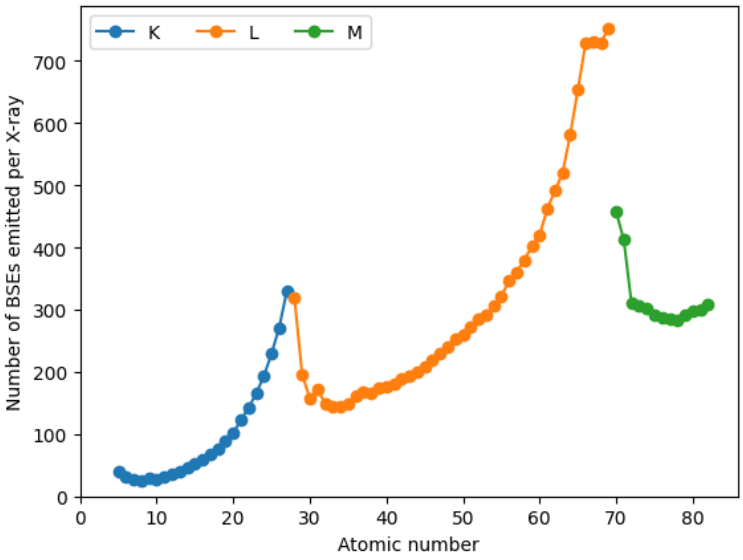

Figure 1. Number of BSEs emitted per X-ray as a function of atomic number for pure samples at an accelerating voltage of 20 keV and a take-off angle of 35º. Only the ratio for the most intense X-ray line series is shown (K, L or M). The BSE yield is calculated based on Love and Scott's parametrisation [5]. The X-ray yield is calculated using the spectrum synthesis engine developed by Statham *et al.* [6].

However, the electron filter also absorbs low energy X-rays, which means that not all elements may be detected depending on the filter thickness. One solution to detect all elements is, therefore, to use a thinner filter and work at lower accelerating voltages (< 12 keV). However, this inevitably results in a decrease X-ray yield due to the lower overvoltage and possibly stronger overlaps between X-ray peaks as high energy X-ray lines are no longer excited and lower energy, closely spaced X-ray lines must be used. Figure 2 shows the calculated X-ray intensity of the most intense line series for pure samples at different accelerating voltages and electron filter thicknesses [12]. C, N and O starts to be detectable with a 3 µm filter and an accelerating voltage of 12 kV [12]. The X-ray intensities of heavier elements decrease at this accelerating voltage due to the lower overvoltage. For example, the calculated X-ray intensity of Fe-K is 809 kcps/nA at 20 kV, which drops to 170 kcps/nA at 12 kV. At 6 kV the line is no longer excited. While the Fe-L can be used, its intensity always remains lower than the Fe-K, due to its emission probability and photoelectric absorption in the sample and in the electron filter. At 20 kV, the Fe-L is barely detectable due to the thick electron filter. Its intensity is 5 kcps/nA at 12 kV and increases to 62 kcps/nA at 6 kV, but still lower than the Fe-K at 12 and 20 kV.

By occupying the same, high solid angle position under the pole piece, the annular EDS detector prevents the use of the normal BSE detector; both detectors cannot be inserted at the same time. As aforementioned, the BSE signal often provides quick and familiar compositional information when navigating around a sample. As shown in Figure 1, the BSE signal will always have

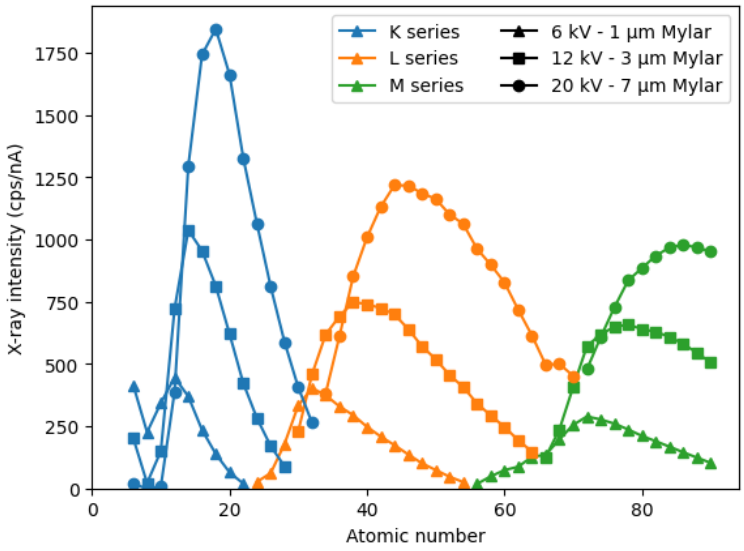

Figure 2. Calculated X-ray intensities at different accelerating voltages and Mylar thicknesses based on [12]. The intensities are based on the spectrum synthesis engine developed by Statham *et al.* [6], assuming a solid angle of 0.78 sr, a Mylar composition of 4.2 wt% H, 62.5 wt% C and 33.3 wt% O and a density of 1.4 g/cm^3 [13]. Only the intensity of the most intense X-ray line series is shown (K, L or M).

a higher signal to noise ratio (S/N) than the EDS signal. For fast and live acquisitions, the BSE signal therefore provides information about the sample (e.g., morphology, phase boundaries, topographical structures) that would take much longer to collect using only EDS.

Soltau *et al.* [9] and then Liebel *et al.* [14] proposed a concept of a combined annular EDS and BSE detector for SEMs, which consists of BSE sensors located around a central hole, and X-ray sensors positioned outside the BSE sensors, as schematically represented in Fig. 3a. In this configuration, BSE and X-ray signals can be simultaneously collected by the same detector, addressing one limitation of the annular EDS detector, but with the downside of a lower solid angle for the X-ray sensors as they are positioned further away from the central hole (c.f., Fig. 3b). As shown in Fig. 4, the solid angle decreases as a function of the distance between the X-ray sensors and the electron axis. While this is partially compensated by larger, elongated X-ray sensors, their response time will be worse than the one of circular, tear-drop shaped sensors, resulting in larger ballistic deficit and reduced throughput [15]. As for the annular EDS detector, this concept would require thinner electron filters and lower accelerating voltages to detect all elements. Note that in both cases, the conventional EDS detector, which could detect all elements, cannot be used because of their size and square shape blocking its line of sight (Fig. 3) [12].

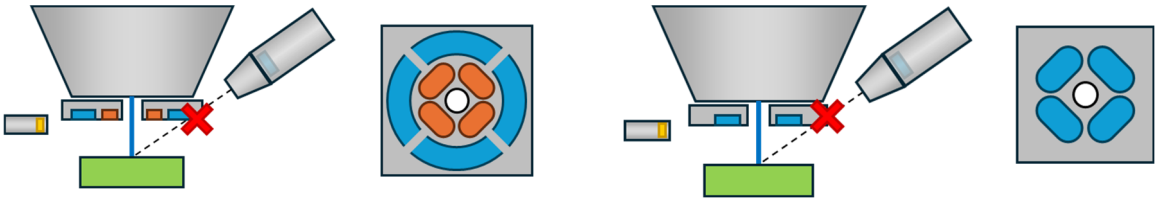

a) b)

Figure 3. Schematic representation of the a) combined annular EDS and BSE detector, and b) annular EDS detector from Soltau *et al.* [9]. X-ray sensors are coloured in blue, whereas BSE sensors appear in orange.

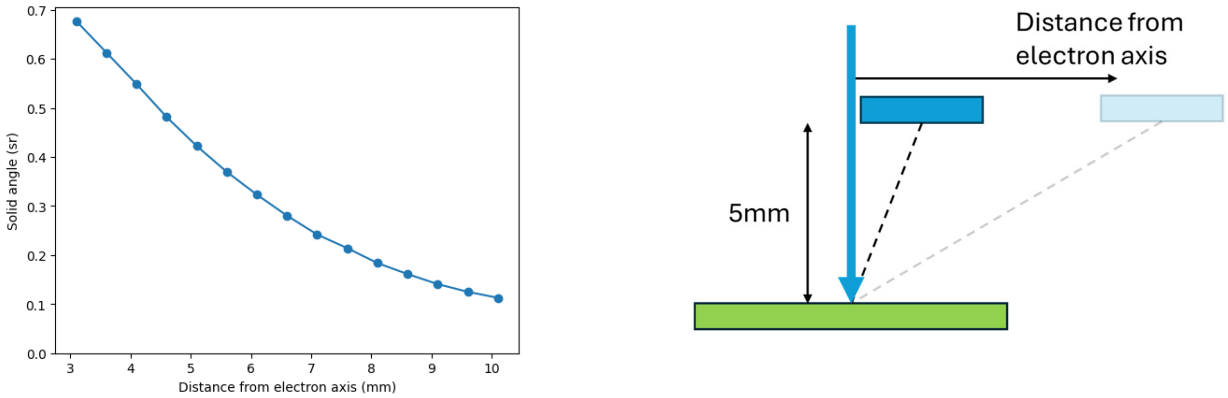

a) b)

Figure 4. A raw spectrum from Drake and Weill [19] glass REE1 along with the residual generated during quantification (5.6×10^7 total counts).

In 2023, we introduced a variation on the concept of an under-the-pole-piece, combined X-ray and BSE detector with the introduction of a backscattered electron and X-ray (BEX) imaging detector. The objective was to provide a solution to help microscopists efficiently analyse their entire sample, using large solid angle BSE and X-ray sensors that give good compositional and topographical contrast for the BSE image, avoid obscuring the line of sight of conventional EDS detectors and yield high X-ray throughput, fast response time and accurate discrimination of materials of different composition. The next paragraphs describe the components of a BEX detector, underlying software algorithms and design choices made during their development. Examples of applications, including comparison to analyses performed with a conventional EDS detector are presented, before some concluding remarks and future outlook.

2. *HARDWARE COMPONENTS*

A BEX detector is made of several components: X-ray sensors, BSE sensors, thermoelectric cooling, head assembly, insertion / retraction arm, motor drive, electronics, etc. The head assembly consists of two X-ray sensors, two BSE sensors, a thermoelectric cooling device and a hole to let the electron beam through. As for annual EDS detectors, an electron filter is used to block electrons, due to the space constraints. A polymeric filter covers the two X-ray sensors and absorbs electrons up to an energy of 20 keV. While high energy X-rays pass through, low energy X-rays below 950 eV are absorbed by the filter. Practically, this means that this detector can detect X-rays of any element from sodium (Z = 11, Na-Kα: 1.041 keV). Each X-ray sensor is also fitted with a collimator to block stray X-rays from the microscope chamber or stage from entering the sensor. The X-ray sensors are positioned as close as possible to the central hole to maximize their solid angle (Fig. 4).

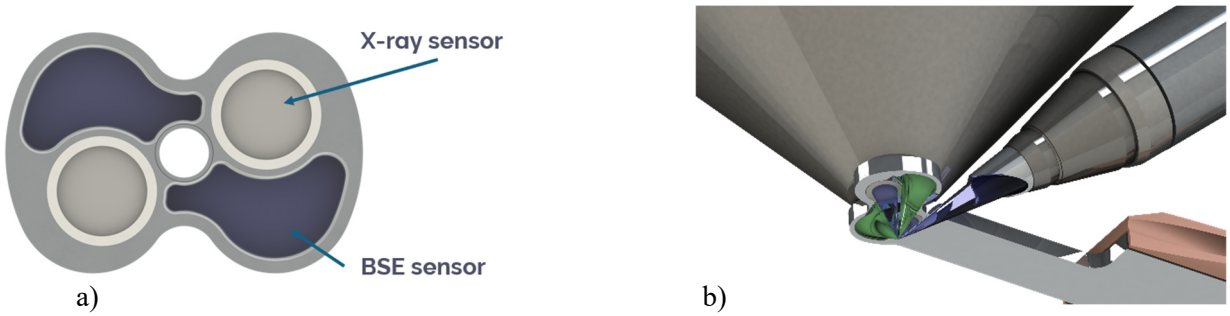

Figure 5. a) Schematic of the head of the BEX detector showing the X-ray and BSE sensors, as well as the cut-outs to allow line of sight of the conventional EDS detectors. b) Schematic showing the positioning of the BEX and EDS detectors inside the microscope chamber.

Conventional semiconductor BSE detectors are usually made of two or four segments arranged around a central hole. The symmetrical arrangement of the segments is important for compositional imaging (i.e., Z-contrast). The angular distribution of emitted BSEs depends on the surface tilt [16], therefore, more BSEs will be emitted in a particular direction depending on the surface tilt and some segments will detect a stronger BSE signal than the others. Only if the segments are symmetrically positioned with respect to the electron beam, will the aggregated signal of all segments produce a signal proportional to the atomic number. The integration of X-ray sensors in the head means that a new positioning of the BSE sensors was required. Furthermore, another constraint on the position and shape of the BSE sensors is the line of sight of the side-mounted, conventional EDS detector. As the BEX detector cannot detect light elements due to its electron filter, the EDS detector with a conventional electron trap can be used in tandem to measure all elements from Be to Cf. This however means that the side-mounted detector(s) cannot be occluded by the BEX head. Through theoretical calculations, computer-aided designs and experimental prototypes, the position of the X-ray sensors, BSE sensors and cut-outs were refined to finally arrive at the arrangement seen in Fig. 5.

The two BSE sensors are symmetrically positioned with respect to the electron beam and have a large collection area to offer good BSE signal sensitivity at low beam currents. Two cut-outs on either side of the head give full line of sight to two conventional EDS detectors, each up to a sensor area of 170 mm^2.

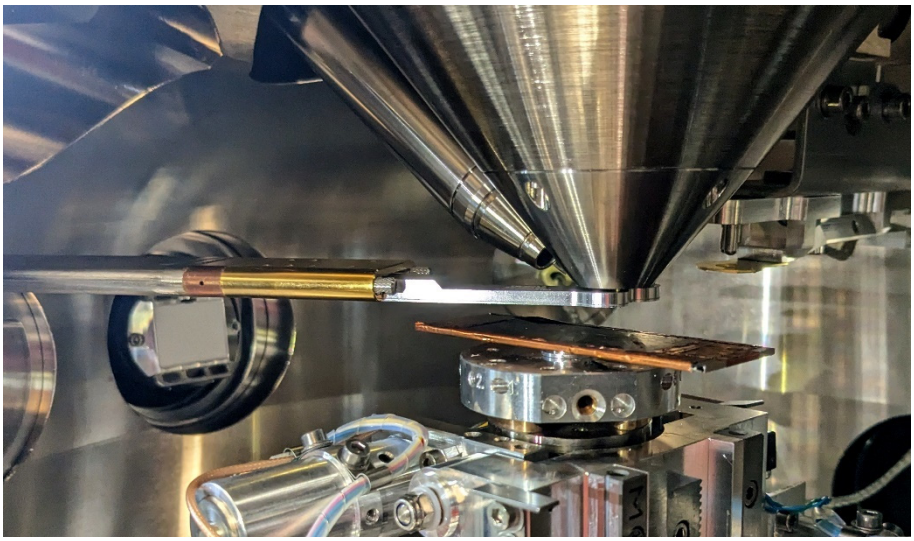

Figure 6. View inside of the microscope chamber showing the inserted EDS and BEX detectors. The flat profile of the arm of the BEX detector gives freedom of movement over large samples like a thin section.

The thermoelectric device (Peltier) cools both X-ray and BSE sensors to a stable temperature during operation of the BEX detector. Cooling and a stable temperature are required to achieve good X-ray performance. The heat is transferred outside the microscope chamber by a heat pipe inside the arm to a heat sink in the external body. The size of the hole was selected to allow acquisitions at low magnification, and consequently large area mapping of whole samples. For a working distance of 8.5 mm, the largest field of view is approximately 2 mm without any occlusion from the hole and any non-uniformity in the X-ray and BSE signals. The profile of the arm was designed so there is nothing protruding below the plane of the head. This allows large samples, like geological thin sections, to be analysed without any risk of hitting the BEX detector when moving the stage (Fig. 6).

3. SOFTWARE ALGORITHMS

During a map acquisition, multiple signals are simultaneously processed, stored, and displayed, as schematically shown in Fig. 7. Four signals are outputted from the BEX detector: two X-ray signals and two BSE signals. As for conventional EDS detectors, the energy of each individual

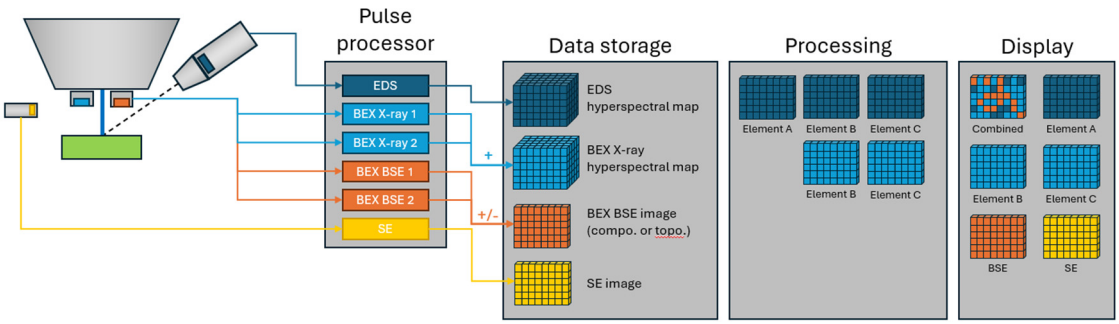

Figure 7. Schematic illustrating the signal processing, storage and display of data collected during a combined BEX and EDS acquisition.

X-ray entering either BEX X-ray sensor is converted to a voltage signal via the ionisation of the Si atoms in the semiconductor crystal, amplified by the field effect transistor, detected by the discriminator channels of the pulse processor, and measured using a processing time to extract the energy of the voltage jump [15]. This process is independently performed for the two X-ray sensors in the BEX detector, as well as the signal coming from the conventional EDS detector.

Independent processing channels mean that different processing times can be used for the BEX X-ray and conventional EDS signals. For instance, the conventional EDS detector will always have a smaller solid angle than the BEX X-ray sensors, thus a lower count rate. This allows a longer process time to be used, which is particularly well-suited to analyse light elements by improving the spectral resolution and consequently the deconvolution of X-ray peaks in the low energy range of the spectrum. As the BEX X-ray signals have no low energy X-ray events due to the electron filter, the spectral resolution is less critical, and using a shorter process time increases the throughput to fully utilise the higher solid angle of the BEX X-ray sensors.

The result of the pulse processor is a series of X-ray events with their associated X-ray energies, which is then sent to the PC for storage and processing. At this stage, the signal of the two BEX X-ray sensors are combined into a single data storage, i.e., a hyperspectral map of dimensions equal to the width and height of the field of view and depth of the number of channels (typically 2,048 channels). The X-ray events from the conventional EDS detector is separately stored in its own hyperspectral map. This data storage strategy has a few advantages. First, the BEX and EDS detectors have different take-off angle, element detection capability and spectral resolution. Keeping their signal separate in the data storage allows to tailor the spectral processing to the characteristics of each detector. For instance, different peak profiles are generated based on the detector efficiency, resolution, and geometry of each detector [17-19], which allows for a better deconvolution of overlapping peaks and extraction of their X-ray intensities. Secondly, the BEX and EDS detectors may detect different elements from the sample. On one hand, the BEX detector cannot measure elements below Na due to the electron filter, and on the other, the conventional EDS detector may not collect any X-ray from certain areas of the sample due to

topography and its shallower elevation angle (e.g., particle inside a crack). Separate hyperspectral maps allow for the adjustment of the list of elements used for spectral processing of each detector. Finally, aggregating the signals from the BEX X-ray sensors improves the S/N ratio as each pixel spectrum in the hyperspectral map contains more counts. Two BSE signals, one for each BSE sensor, are transmitted to the pulse processor. Depending on the imaging mode, compositional or topographic, the two signals are added or subtracted, and then amplified to produce the final BSE image. The amplification depends on the specified gain and offset, which could either be manually adjusted or automatically optimised by a calibration routine before the acquisition. At the same time as the EDS, BEX X-ray and BEX BSE signals are acquired, the signal from the SE detector of the microscope is also collected by the pulse processor and transferred to the PC for storage. In total, at least 5 different signals are handled by the pulse processor during a map acquisition and stored on the PC.

Figure 8 shows an example of a map acquisition with BEX and EDS. Note that the C-K and O-K maps are only available for the conventional EDS detector, whereas Si-K, Cu-K, Zn-K and Pb-M maps are available for both detectors. Spectral processing was done separately but simultaneously on both hyperspectral maps by filtering the background using a top-hat filter and extracting the net intensities using a least-squares fit of calculated peak profiles [20, 21]. The profiles of C-K, O-K, Cu-L, Zn-L, Si-K, Pb-M, Cu-K, Zn-K and Pb-L were considered for the conventional EDS detector, whereas only the profiles for Si-K, Pb-M, Cu-K, Zn-K and Pb-L were used for the BEX detector. To improve processing speed, some profiles can be excluded by pre-selecting the detector, which will yield the elemental map with the highest intensities for each element. The pre-selection relies on the detector efficiency, geometry, and relative solid angle between the two detectors. In this example, there is no need to fit the Si-K, Pb-M, Cu-K, Zn-K and Pb-L profiles for the conventional EDS detector, as the Si, Pb, Cu and Zn elemental maps from the BEX detector will contain more counts, as can visually be observed in Fig. 8. As for conventional EDS mapping, the storage of the hyperspectral maps allows adding and removing elements during post-processing and regenerating net intensity elemental maps based on the selected elements.

4. APPLICATIONS

Figure 9 shows a screen shot during a live chemical imaging [22] investigation of a granite sample while moving the sample and scanning live at a frame rate of 5 frames per second. The results were collected using a S8000 FEG-SEM (Tescan, Czech Republic) equipped with an UltimMax 170 EDS detector, a Unity BEX detector and AZTECLIVE 6.1SP1 software (Oxford Instruments NanoAnalysis, UK). It shows a comparison between BEX imaging in Fig. 9a and the traditional BSE imaging in Fig. 9b; the two images were collected simultaneously under the same conditions. It highlights the differences between the two imaging modes and the limitations of the BSE mode as explained in the introduction. On one hand, the BSE image in grey level shows an indicative information about the different phases present through the variations in

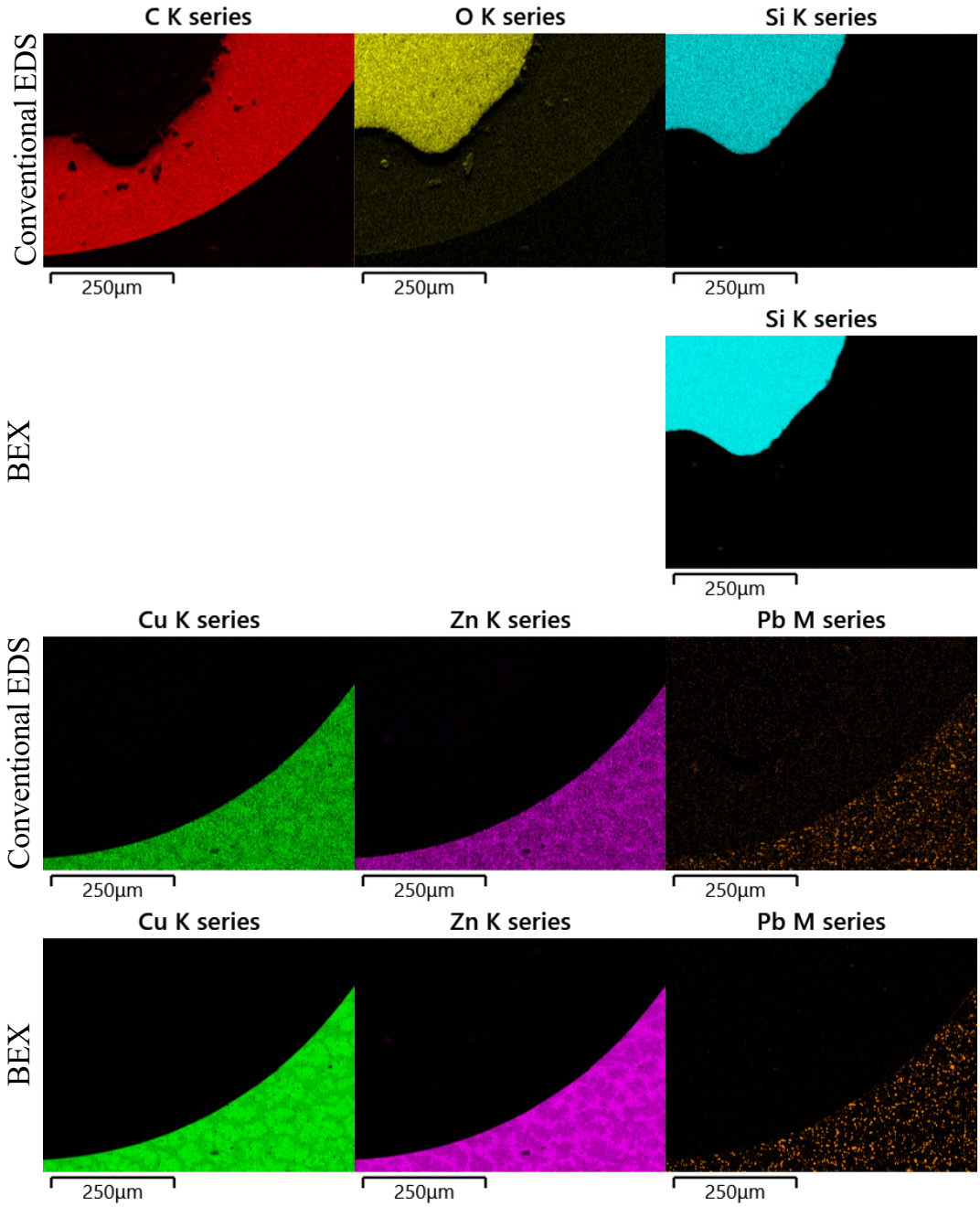

Figure 8. Net intensity elemental maps of C, O, Si, Cu, Zn and Pb for a combined BEX and EDS mapping acquisition at 20 kV on the edge of a SiO_2 sample mounted in a brass standard block.

atomic numbers and on the other hand, the BEX image, which is the combination of BEX-BSE and BEX-X-ray, shows a coloured image emphasising the main elements present in the scanned area with a corresponding legend. This allows the user to find areas of interest and specific phases quickly and reliably while navigating around the sample.

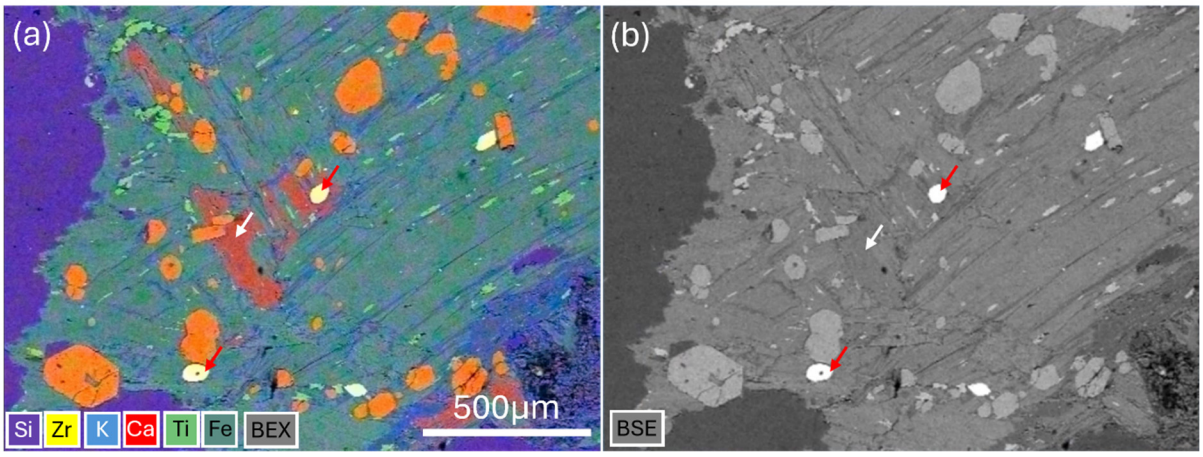

Figure 9. Comparison between a) live BEX imaging, and b) live BSE imaging at a frame rate of 5 frames per seconds on a granite sample (accelerating voltage of 20 kV and beam current of 1.5 nA). Both data were collected simultaneously under the same conditions using a BEX detector.

When relying on only the BSE signal, phases with small atomic number differences can be easily missed. This is demonstrated in this example with the calcium-rich phase, highlighted with a white arrow in Fig. 9, which is indistinguishable from the iron-rich phase in the BSE image (green phase in BEX image). In addition, one can note the limitation of the BSE signal to separate small and large atomic number differences at the same time. In this example, the zirconium-rich phase, indicated with red arrows, is saturated in the BSE image. Any phase with higher atomic number will also appear white and thus cannot be distinguished in the BSE image.

The results in Fig. 10 show an analysis of a non-polished, non-coated drilled gemstone sample using a SU3500 W-SEM (Hitachi, Japan) in low vacuum mode equipped with UltimMax 100 EDS detector and Unity BEX detector (Oxford Instruments, UK). The aim of the analysis is to check the authenticity of the gemstone by analysing its interior. The EDS, BEX X-ray and BSE data were collected simultaneously, as previously explained, using an accelerating voltage of 20 kV and a beam current of approx. 3 nA. Working with a non-polished sample and in variable pressure mode makes the analysis particularly challenging for EDS.

The topography of the sample and shallow take-off angle of the EDS detector makes it impossible to analyse the inside of the gemstone solely with the EDS signal, as shown in Fig. 10a. Furthermore, the large variation in the sample height induces changes in the working distance, which may lead to reduced EDS signal due to the detector collimator. The geometry of the BEX detector, immediately above the sample, translates into a high take-off angle and less sensitivity to topography and collimation effects, as shown in Fig. 10c where elemental information can be observed from inside the holes of this sample.

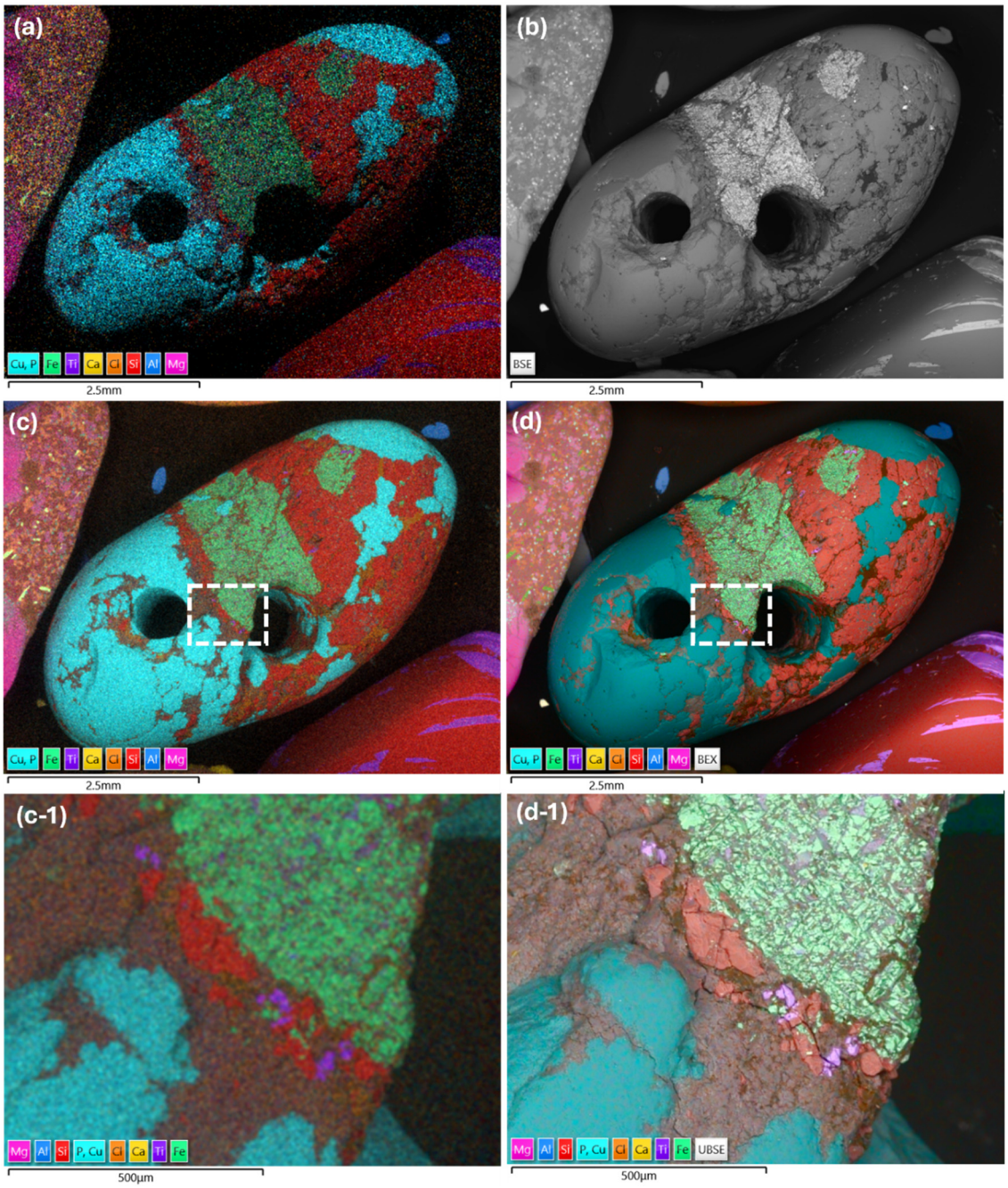

Figure 10. Comparison between a) conventional EDS map, b) BEX X-ray map, c) BSE, and d) BEX combined BSE and X-rays image. b-1) and d-1) are magnified images from dashed rectangle in b) and d) respectively. All data was collected simultaneously under the same conditions using conventional EDS and BEX detector (accelerating voltage of 20 kV and approx. 3 nA).

Figures 10a and 10c show the comparison between EDS and BEX X-ray maps for the same acquisition time. The BEX X-ray map (Fig. 10c) has about 12 times more signal compared to EDS map (Fig. 10a) resulting in a more detailed map. Another advantage of the large solid angle of the BEX X-ray sensors is the ability to reduce the beam current for the acquisition and consequently the beam diameter. Even for FEG-SEM, the best spatial resolution is achieved at

low beam currents and high accelerating voltages [23, 24]. The ability of BEX to operate at lower beam currents (typically 1 - 4 nA) than conventional EDS and high accelerating voltages (20 kV) means sharper, higher resolution images.

Figure 10d shows the resulting BEX image, combining BEX-BSE (Fig. 10c) and BEX-X-ray maps (Fig. 10b). The resulting BEX image benefits from the low noise in the BSE image, which adds valuable topographical and structural information due its higher spatial resolution compared to X-ray. This is shown in the comparison between the X-ray data in Fig. 10b-1 and the BEX data in Fig. 10d-1. The combination of the two signals, BEX image, results in a sharp, low noise, coloured image embedded with elemental information.

Figure 11 shows an automated whole sample investigation of a 3D printing powder mounted on a 12 mm aluminium stub. The analysis, aimed at detecting contaminants within the powder mixture, was performed on SU3800 W-SEM (Hitachi, Japan) using an UltimMax 65 EDS detector and Unity BEX detector (Oxford Instruments, UK). The large area mapping was acquired in 30 minutes and resulted in a dataset of 88 million pixels covering an area of 128 mm^2 with a resolution of 1.4 µm. 432 separate fields were collected and stitched together to form a cartography of the whole sample as presented in Fig. 11a. The powder is made of aluminium in blue and nickel in green. A few titanium contamination particles, labelled in red and as small as 5 µm, were detected in the sample (Fig. 11b). A typical analysis of such sample with a conventional EDS detector would take several hours depending on the sensor size and would be susceptible to shadowing artefacts (e.g., some contaminant particles might be invisible if located next to larger particles on the opposite direction of the EDS detector). In addition to the increase in throughput and sensitivity, the analysis is accelerated by the simultaneous collection of signals (SE, BSE and X-ray from BEX and EDS). In other words, each field is only scanned once, in comparison to the previous workflow where an electron image was first collected then followed by a second, slower scan for the EDS map.

5. CONCLUSION

In various ways, backscattered electron and X-ray imaging is the realisation of the complementary nature of the BSE and X-ray signals. By itself, the BSE signal cannot provide unambiguous information about the chemical element content and distribution of a sample due to the limited dynamic range and atomic number sensitivity of the BSE detector. Conversely, the X-ray signal will always have a worse S/N than the BSE signal due to the low ionisation cross-sections. By increasing the solid angle of the X-ray sensors, giving line of sight to the conventional EDS detector so all elements can be detected, while simultaneously acquiring all signals, BEX expands the capabilities of SEMs and unlocks new workflows to accelerate the analysis of samples in the SEM, notably using live chemical imaging and cartography of the whole sample.

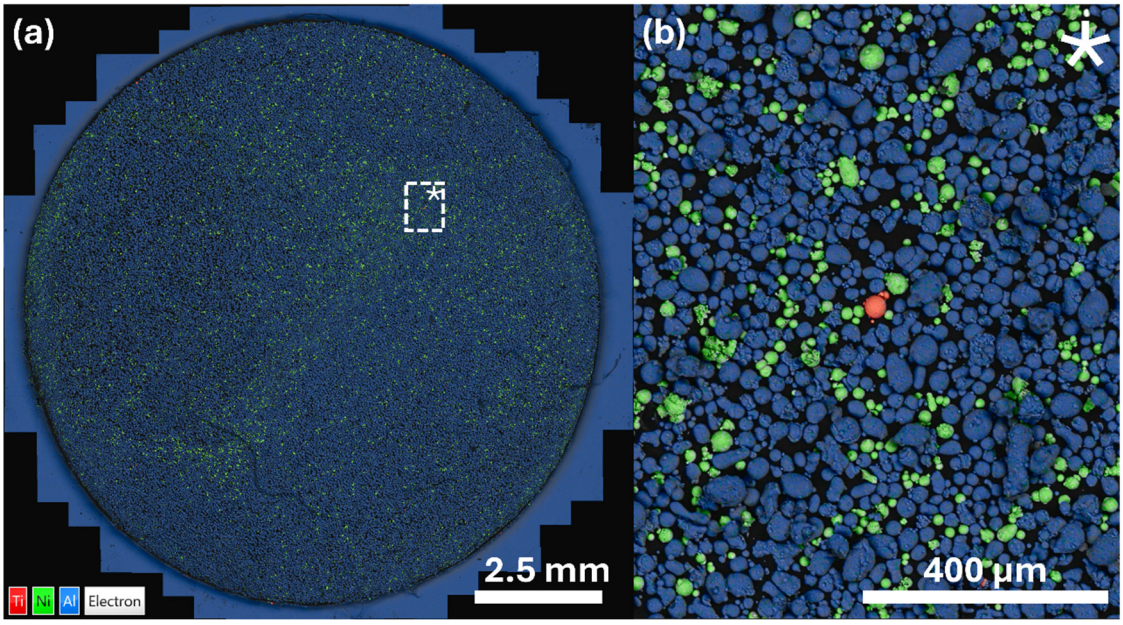

Figure 11. Large area mapping of a 3D printing powder sample using BEX. a) Overview of the entire sample, and b) enlarged subset showing the individual powder particles and the resolution of the acquisition.

6. *ACKNOWLEDGMENTS*

The authors would like to acknowledge Susumu Yamaguchi (Oxford Instruments) for the acquisition of some of the data presented in this manuscript.

7. *REFERENCES*

[1] Collins C L, *et al.* 2009 *Microsc. Microanal.* **15** (Suppl. 2) 172
[2] Niculae A, *et al.* 2016 *Microsc. Micronal.* **22** (Suppl. 3) 42
[3] Burgess S, *et al.* 2017 *Microsc. Microanal.* **23** (Suppl. 1) 46
[4] Niculae A, *et al.* 2023 *Microsc. Microanal.* **29** (Suppl. 1) 2087
[5] Love G and Scott V 1978 *J. Phys. D* **11** 1369
[6] Statham P J, *et al.* 2016 *IOP Conf. Ser.: Mater. Sci. Eng.* **109** 012016
[7] Xiaobing L, *et al.* 2013 *Microsc. Microanal.* **19** (Suppl. 2) 1136
[8] Terborg R, *et al.* 2010 *Microsc. Microanal.* **16** (Suppl. 2) 1302
[9] Soltau H, *et al.* 2009 *Microsc. Microanal.* **15** (Suppl. 2) 204
[10] Teng C, *et al.* 2018 *Microsc. Microanal.* **24** 238
[11] Terborg R, *et al.* 2017 *Microsc. Today* **25** 30
[12] Brostrom A, *et al.* 2020 *Microsc. Microanal.* **26** 373
[13] Berger M J, *et al.* 2017 *NIST Standard Reference Database* **124**
[14] Liebel A 2014 *Microsc. Microanal.* **20** (Suppl. 3) 1118

[15] Oxford Instruments NanoAnalysis 2023 *Silicon drift detectors explained*. [High Wycombe, UK: Oxford Instruments NanoAnalysis]
[16] Andrea M, *et al.* 1996 *Scanning* **18** 401
[17] Statham P J 2009 *Microsc. Microanal.* **15** 528-529
[18] Statham P J 2010 *Microsc. Microanal.* **16** 1304-1305
[19] Pinard P T, *et al.* 2020 *IOP Conf. Ser.: Mater. Sci. Eng.* **891** 012020
[20] Statham P J 1977 *Anal. Chem.* **49** 2149-2154
[21] Statham P J 2002 *J. Res. Natl. Inst. Stand. Technol.* **107** 531
[22] Pinard P T, *et al* . 2018 *Microsc. Microanal.* **24** (Suppl. 1) 624
[23] McSwiggen P 2014 *IOP Conf. Ser.: Mater. Sci. Eng.* **55** 012009
[24] Pinard P T and Richter S 2014 *IOP Conf. Ser.: Mater. Sci. Eng.* **55** 012016